Measurements of the Thickness of Liquid Films Utilizing Total Reflection of a Laser Beam at the Phase Boundary

Sebastian Blessing[1,*], Steven Wagner[2], Jochen Kriegseis[1]

1: Institute of Fluid Mechanics (ISTM), Karlsruhe Institute of Technology (KIT), Germany
2: Institute for Reactive Flows and Diagnostics, Technical University of Darmstadt, Germany
*Corresponding author: sebastian.blessing@kit.edu

Keywords: Film Thickness, Refractive Index, Liquid Films, Two Phase Flow, Image Processing

ABSTRACT

In this work, a measurement technique for measuring liquid film thickness based on the total reflection of a laser is investigated. The thickness of liquid films is a key parameter in modeling certain two-phase flow regimes like annular or slug flow. Its measurement usually requires extensive optical or mechanical access to the flow. However, in situations where optical access is limited and radical modifications on the measurement object are impossible, e.g. in an operating fuel cell, these conventional techniques are not easily applicable. A key feature of the technique presented in this work is that it requires no modifications other than an optical access at the surface on which the liquid film of interest is deposited on. A laser beam is introduced through a prism to the optical access and consequently the liquid film in an angle that causes the beam to be totally internally reflected at the free surface of the film. An imprint of the reflected beam, which leaves the optical access again through the prism, is captured on a scope. If the thickness of the film changes, the laser beam's optical path changes with it, causing a displacement of its imprint on the scope. This displacement is a direct measure for the film thickness. In this work, a three dimensional linear algebra model describing the experimental setup is presented and used to derive the basic working principle. It is successfully shown in a proof of concept study that the measurement technique correctly estimates the thickness of a static liquid film deposited on a prism in combination with a cross-correlation based image processing routine. To understand the restrictions of the measurement technique, the most important error sources with regards to the measurement of dynamic film flows are discussed using a mixed analytical and numerical approach based on the previously derived working model. The technique is likely applicable to dynamic film flows. However, concerns regarding high measurement uncertainty caused by curved free surfaces demand further investigation.

1. Introduction

Measuring the thickness of liquid films is a key challenge in understanding phase-change phenomena for all two-phase flow regimes in which a coherent film of liquid can form at a solid boundary. These include annular and slug flow regimes (as described by Suo & Griffith, 1964) observed in mini or micro channels, which are shown in Fig. 1.

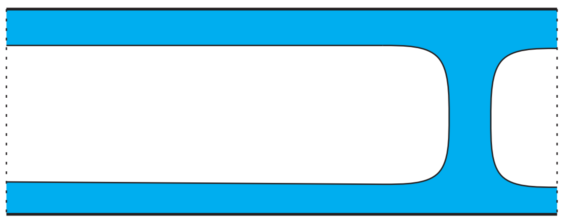

(a) slug flow

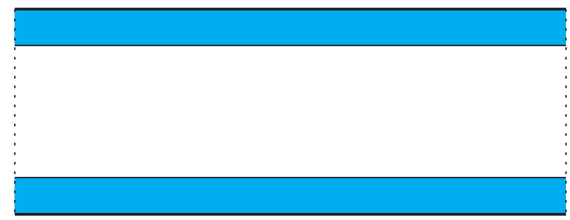

(b) annular flow

Figure 1. Two-phase flow regimes with films according to Triplett et al. (1999) (white - gas phase; blue - liquid phase).

Several solutions are available when direct access to the free surface between air and film is possible. One simple, mechanical approach is to bring a needle in contact with the liquid film surface and record its deflections (Takahama & Kato, 1980).

Multiple mostly non-intrusive electrical film thickness measurement approaches have been proposed. The most popular is the capacitive approach (Takahama & Kato, 1980; Klausner et al., 1992; Ameur et al., 2007; Liu et al., 2007), where the liquid film acts as one electrode of a capacitor. Another approach is to utilise the electrical resistance of a liquid film in order to determine its thickness (Coney, 1973; Kang & Kim, 1992; Fukano, 1998; Seleghim & Hervieu, 1998; Kumar et al., 2002; Burns et al., 2003).

Ultrasonic sensors can be used without the need for physical and/or optical access (Lu et al., 1993; Pedersen et al., 2000). One of the main challenges for this technique is the correct estimation of sonic speed in all media the waves travel through.

The broadest class of film thickness measurement techniques, however, are optical techniques, ranging from simple shadowgraphy techniques to elaborate sensors like the laser focus displacement meter. When optical access to the side of the film can be granted, high-speed imaging can be used to measure the film thickness (Moriyama & Inoue, 1996; Aussillous & Quéré, 2000; Barbosa Jr et al., 2001; Ursenbacher et al., 2004). The contrast of the images can be enhanced by adding fluorescent particles to the liquid film (Steinbrenner et al., 2007).

Likewise, but without the requirement of sideways optical access, the intensity of light from fluorescent particles (Makarytchev et al., 2001; Wigger et al., 2016; Schulz et al., 2016) or scattered light from non-fluorescent particles (Salazar & Marschall, 1975) can be used as a measure for film thickness. Light scattering and absorption can also be used by relating the reduction in intensity of the (laser) light, possibly at different wave lengths, passing through the film to its thickness, if the liquid is sufficiently opaque (Mouza et al., 2000; Porter et al., 2011; Lubnow et al., 2021; Schmidt et al., 2021). The liquid can also be mixed with particles or dye to increase the reduction of light intensity per film thickness.

A technique utilising total internal reflection of diffuse light in combination with imaging was presented by Hurlburt & Newell (1996) and extended by Shedd & Newell (1998). The liquid film is deposited on a transparent surface in this method and the light enters the system through this surface. Similarly, light conducting fibers can be inserted into the solid surface (Than et al., 1993;

Yu et al., 1996), where a central one acts as a sender, illuminating the film from the inside, while the others act as receivers. In this case, the distance between the sending fiber and the first receiving fiber determines the film thickness.

Commercially available laser triangulation sensors can be used to measure the thickness of opaque liquid films in the presence of a reflecting background (Peterson & Peterson, 2006; Åkesjö et al., 2018).

The laser focus displacement meter utilises an oscillating objective lens to shift the focal point of a laser beam back and forth continuously (Takamasa & Kobayashi, 2000; Hazuku et al., 2005; Han & Shikazono, 2009, 2010; Han et al., 2011; Busam et al., 2001). When the focal point crosses a phase boundary, the resulting increase in reflected light intensity is registered and the position of the phase boundary can be reconstructed.

A more direct measurement principle - the Laser Pattern Shift Method - that only demands optical access through the surface underneath the liquid film was proposed by Foltyn et al. (2019). Here, a laser pattern is introduced to the film through an underneath-located optical access, appropriately inclined to guarantee total reflection of the pattern at the air-liquid interface. Comparison to a reference position of the laser pattern in absence of the film yields a displacement on a scope, which is proportional to the film thickness. An especially attractive feature of this technique is that, since no modifications to the liquid (e.g. tracer, fluorescence or dye supply) are required for the measurement, the method is particularly advantageous in situations where these modifications are difficult or impossible, such as, e.g., in condensation experiments or operated fuel cells.

The technique as presented by Foltyn et al. (2019) aimed for measuring the lamella thickness of a droplet impinging on a wall and was later extended (Foltyn et al., 2021) to achieve this goal. A core simplification for the derivation of the measurement principle is the assumption that the film surface is parallel to the surface of the optical access. The present work, therefore, aims to explore the possible measurement error caused by deviations from this and further underlying assumptions. Understanding these error sources enables the application of the measurement technique to two phase flow situations with less consistent topology, e.g. slug or annular flow in a mini channel.

Moreover, the presented work provides an overview of the optical fundamentals of the measurement technique and an experimental setup similar to the work of Foltyn et al. (2019) is presented in order to provide example data sets for an enhanced data-processing routine including sub-pixel accuracy and real-time capability.

2. Methodology

To facilitate the discussion of possible error sources, the working principle as derived by Foltyn et al. (2019) is presented here using a three-dimensional linear algebra model based on geometrical optics to enable the analysis of laser beam refraction and deflection in all spatial directions.

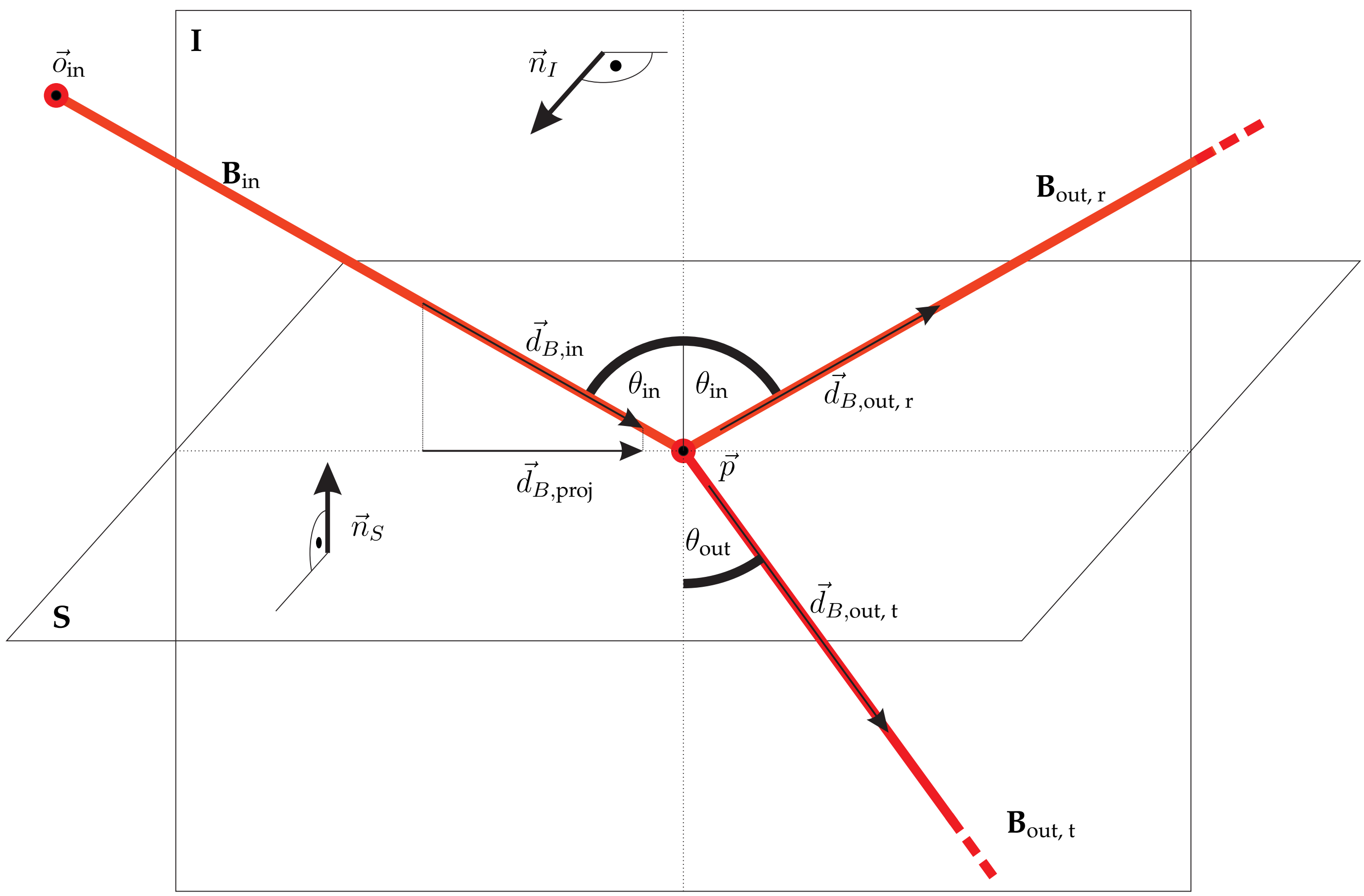

Figure 2. Vector model of a laser beam being reflected or refracted at an optical surface.

The general algorithm for computing the refraction of the laser beam at a surface is briefly described, followed by the derivation of the working principle under the assumption of several simplifications.

The laser beam $\vec{x}$ is described as a line in three-dimensional Cartesian space with origin $\vec{o}$ and direction $\vec{d}$

$$\vec{x} = \vec{o} + a\,\vec{d} \tag{1}$$

and any optical surface is described as a plane in three-dimensional Cartesian space with normal vector $\vec{n}$ and an arbitrarily chosen point on the plane $\vec{x}_0$

$$(\vec{x}_0 - \vec{x}) \cdot \vec{n} = 0. \tag{2}$$

If $\vec{x} \cdot \vec{n} \neq 0$, i.e. the laser beam does not run parallel to the surface, the following steps are undertaken to compute the refraction of the beam B_{in} at the surface S under the angle θ_{in}, moving from a medium with refractive index n_{in} to a medium with refractive index n_{out} as depicted in Fig 2.

1. Compute the intersection point $\vec{p}$ between B_{in} and S.

2. Determine the intersection plane I with its normal vector n_I being the cross product between the directions of the beam and the surface's normal vector $\vec{n}_S$ ($\vec{n}_I = \vec{d}_{B,\text{in}} \times \vec{n}_S$) and $\vec{x}_{0,I} = \vec{p}$.

3. Determine θ_{in} between $\vec{B}_{\text{in}}$ and n_S.

4. Calculate the angle after refraction by Snell's law (Peatross & Ware, 2021, p.75).

$$\theta_{\text{out}} = \arcsin\left(\frac{n_{\text{in}}}{n_{\text{out}}}\sin\theta_{\text{in}}\right) \tag{3}$$

If $(n_{\text{in}}/n_{\text{out}})\sin\theta_{\text{in}} > 1$, the inverse sine function is not defined and θ_{in} is therefore larger than the critical angle θ_{crit} at which total reflection first occurs (Peatross & Ware, 2021, p.81).

5a. $(n_{\text{in}}/n_{\text{out}})\sin\theta_{\text{in}} < 1$: Rotate the direction vector $\vec{d}_{B,\text{in}}$ of B_{in} by $\theta_{\text{in}} - \theta_{\text{out}}$ around the intersection plane's normal vector $\vec{n}_I$.

5b. $(n_{\text{in}}/n_{\text{out}})\sin\theta_{\text{in}} > 1$: Reverse the surface-normal component of $\vec{d}_{B,\text{in}}$.

After following these steps, the beam after the surface is

$$B_{\text{out}} : \vec{x}_{\text{out}} = \vec{p} + a\,\vec{d}_{B,\text{out}}. \tag{4}$$

For the derivation of the measurement principle, the setup is simplified in accordance to Foltyn et al. (2019) by assuming that the problem is two-dimensional and the laser's angle of incidence when first meeting the prism surface is $\theta_{\text{in}} = 0°$.

Figs 3a and 3b show a sketch of the simplified measurement setup without and with a water film respectively. It consists of a prism, a transparent layer (i.e. optical access), and optionally the film layer that is to be measured. For this derivation, additional layers, e.g. coupling media like glue or light conducting gel, between the optical components are neglected.

The surfaces the laser passes through are the prism's front face, the surface between prism and transparent material, the surface between transparent material and film material, the film's top surface and the prism's back face. Since $\theta_{\text{in}} = 0°$ is assumed, the prism's front and back face do not refract the beam and are therefore omitted in this derivation. The surface between prism and transparent material, the surface between transparent material and film and the film's top surface are assumed to be parallel with respect to each other. All quantities relevant for this derivation are presented in Fig. 3c. For the description of the angle relations, angles of incidence on an interface between two media will be denoted as $\theta_{i,j}$, where the direction of the beam is defined as $i \to j$ (**p**rism, **t**ransparent material, **f**ilm material, **a**ir). Therefore, n_i denotes the relevant refractive index for $\theta_{i,j}$.

The laser beam can first be refracted at the interface between prism and transparent surface. Assuming that $n_p = n_t$, i.e. that the transparent material and the prism share the same refractive index, this refraction is also neglected, yielding $\theta_{t,p} = \theta_{p,t} = \theta_{\text{prism}}$.

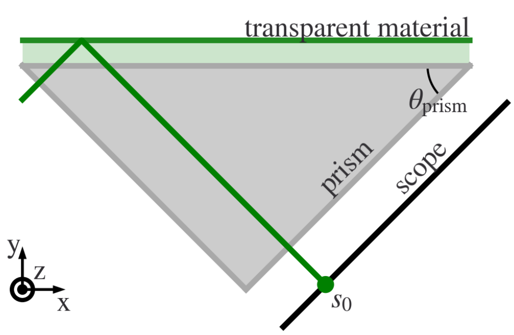

(a) Reference case

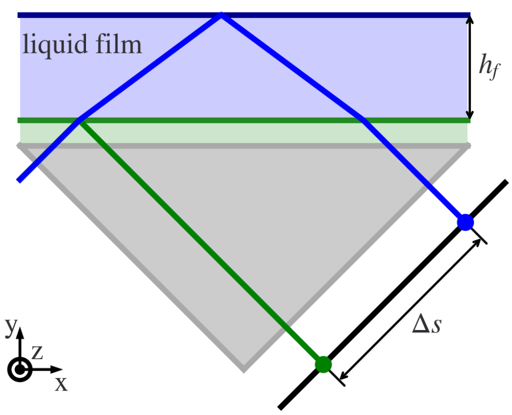

(b) Case with water film

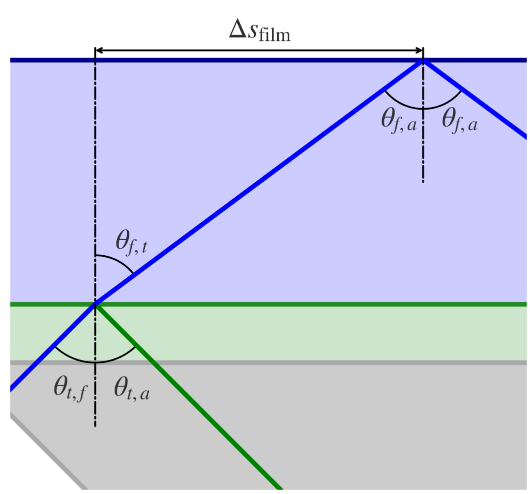

(c) Relevant angles

Figure 3. Two-dimensional sketch of measurement principle

As long as no film is deposited on the solid surface, the laser beam reaches the free surface between transparent material and air and is internally reflected there (Fig. 3a), projecting a reference point s_0 onto an arbitrarily chosen reference plane that is considered to be parallel to the prism's back face.

Therefore, $\theta_{t,a} = \theta_{t,p} > \theta_{t,a,\text{crit}}$ must be given for the measurement principle to be applicable where

$$\theta_{t,a,\text{crit}} = \arcsin \frac{n_a}{n_t} \quad \text{for} \quad n_t > n_a. \tag{5}$$

Now, a film is deposited on the transparent material as depicted in Fig. 3b. The solid-gas interface between air and transparent material is accordingly replaced by solid-liquid and liquid-gas interfaces. In order to remain consistent in notation, the angle of incidence when exiting the transparent material is consequently renamed $\theta_{t,f} \equiv \theta_{t,a}$.

Continued application of the presented algorithm yields

$$\sin \theta_{f,t} = \frac{n_t}{n_f} \sin \theta_{t,f} \tag{6}$$

as the relation between the angle of incidence inside the transparent material and the angle of the laser beam inside the film. Note that the measurement principle is applicable only if

$$\theta_{f,t} < \theta_{f,t,\text{crit}} \Leftrightarrow \frac{n_t}{n_f} \sin \theta_{t,f} < 1. \tag{7}$$

Since $\theta_{f,a} \equiv \theta_{f,t}$, Eq. (6) is inserted in Eq. (7), which results in

$$\frac{n_f}{n_a} \sin \theta_{f,a} = \frac{n_f}{n_a} \sin \theta_{f,t} = \frac{n_f}{n_a} \frac{n_t}{n_f} \sin \theta_{t,f} = \frac{n_t}{n_a} \sin \theta_{t,f}. \tag{8}$$

Interestingly, Eq. (8) reveals that the condition for total internal reflection ($\frac{n_t}{n_a} \sin \theta_{t,f} > 1$) at the free surface between film and air is independent of the material properties of the film for the given setup.

If the above-mentioned reflection condition is met, the beam is reflected at the free surface between water and air. The extended optical path length and deflection lead to a displacement of the point of incidence of the laser on the chosen measurement plane. The magnitude Δs of this displacement is directly related to the thickness h of the water film via

$$h_f = \frac{\Delta s}{2 \cos \theta_{\text{prism}}} \left(\tan \theta_{f,t} \right)^{-1} = \frac{\Delta s}{2 \cos \theta_{\text{prism}}} \left(2 \tan \left[\arcsin \left(\frac{n_t}{n_f} \sin \theta_{t,f} \right) \right] \right)^{-1}, \tag{9}$$

where

$$\Delta s = 2 \Delta s_{\text{film}} \cos \theta_{\text{prism}}. \tag{10}$$

Therefore, it is possible to measure the thickness of a given film without calibration, given that the assumptions made in this section are true and the refractive indices of all media the laser beam passes through are known for the laser wave length λ.

It should be noted that, although this study aims to measure the thickness of liquid films, the principle can also be applied to any transparent solid film.

3. Experimental Setup

The experimental setup for proof-of-concept measurements is built to resemble the theoretical treatise in Fig. 3 as closely as possible. A He-Ne laser with a wave length of $\lambda = 633\,\mathrm{nm}$ and a beam diameter of $3\,\mathrm{mm}$ is used. The laser points upwards in a $45°$ angle in order to perpendicularly enter a symmetrical right triangular PMMA prism. For the current proof-of-concept setup, no problems caused by the laser light reflecting back from the prism into the laser were observed. In further development, however, the angle of incidence will be adjusted to be slightly different from 0 degree to prevent possible issues like interference between the original beam and the beam reflected back into the source. Initially, no additional transparent material is placed on top of the prism so that all indices t in the derivation of the measurement model in Sec. 2 can also be interpreted as those of the prism (p). For the material combination of PMMA and air, and the chosen laser wave length, Eq. (5) yields the critical angle of $\theta_{C,p,a} \approx 42.2°$. The film material used is water, yielding $\theta_{C,p,f} \approx 63.44°$, which confirms the applicability of the chosen combination of materials for the feasibility study.

Opposite of the laser, a scope is placed to represent the measurement plane. It is arranged to be parallel to the top side plane of the prism, as indicated in Fig. 3b. The scope is filmed by a pco.pixelfly usb CCD camera with a dynamic range of $14\,\mathrm{bit}$ grayscale. An AF Nikkor 35mm 1:2D lens is mounted to the camera and focused onto the scope.

When another transparent, solid layer is placed on top of the prism, a laser beam will likely be reflected at the boundary instead of being transmitted as a thin layer of air remains between the two bodies. Therefore, in the present study, a thin layer of ultrasonic gel is applied as a coupling medium between solid layers in order to guarantee the transmission of the beam.

The setup is depicted in Fig. 4. The test rig is leveled so that the top plane of the prism is perpendicular to the direction of gravity, in order to ensure a parallel surface of the liquid film. This is important since the static liquid films considered in this feasibility study are only dependent on gravity and surface tension. Therefore, an angular misalignment causes a systematic error that is investigated, among others, in Sec. 5.

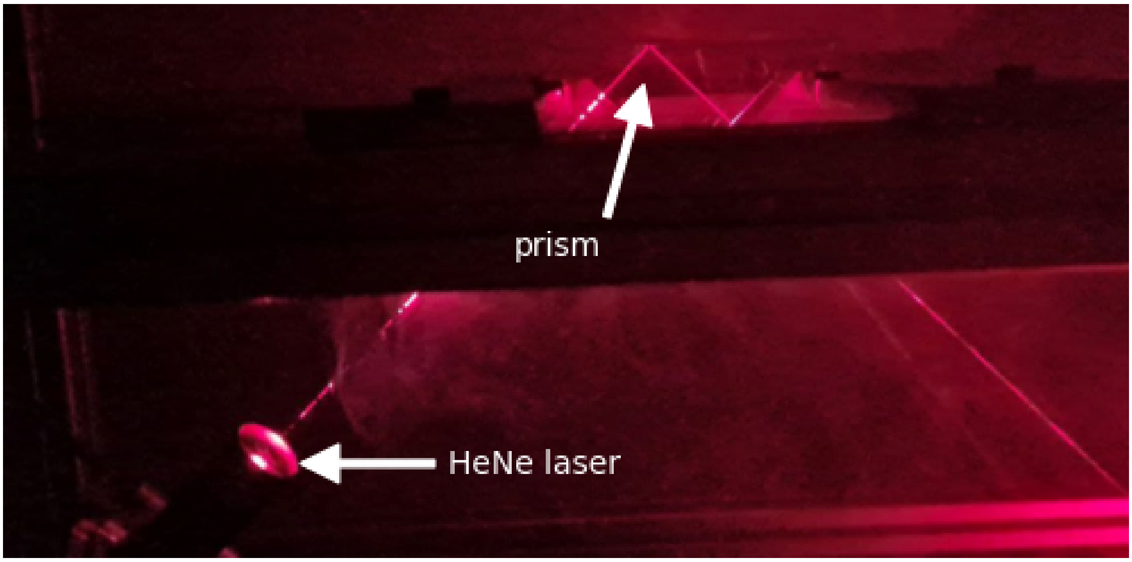

Figure 4. Experimental setup with visualised laser-beam trajectory (reference case; cp. Fig. 3a).

4. Data Processing

In this section, a brief overview over the data processing routine including implications for measurement uncertainty and real-time applicability is given. The processing scripts including the example data set used are available on GitHub (Blessing, 2022).

In order to test the setup described in Sec. 3, a set of images is recorded that show the point of incidence of the laser beam on the scope. The set consists of

- a background / calibration image,
- a reference image where a $4\,\mathrm{mm}$ PMMA plate is placed on a prism with a thin layer of ultrasonic gel as a coupling medium and
- a measurement image where a water film is deposited on the PMMA plate.

A reference shadowgraphy recording of the static film, taken from the side at the same time as the measurement image, with $10\,\mathrm{px/mm}$ (Fig. 5) yields a thickness of $h_{\mathrm{ref}} \approx 3.1\,\mathrm{mm}$.

Fig. 6a shows the reference beam position to the left and the measurement beam position displaced by the propagation and subsequent reflection in the liquid film to the right. It is evident from the image that the beam displaced by the film maintains the characteristic Gaussian shape. Therefore, to compute the displacement between the beams, an algorithm based on image cross-correlation can be used, which is outlined in the following.

1. Transform the images into the frequency domain using the two-dimensional fast Fourier

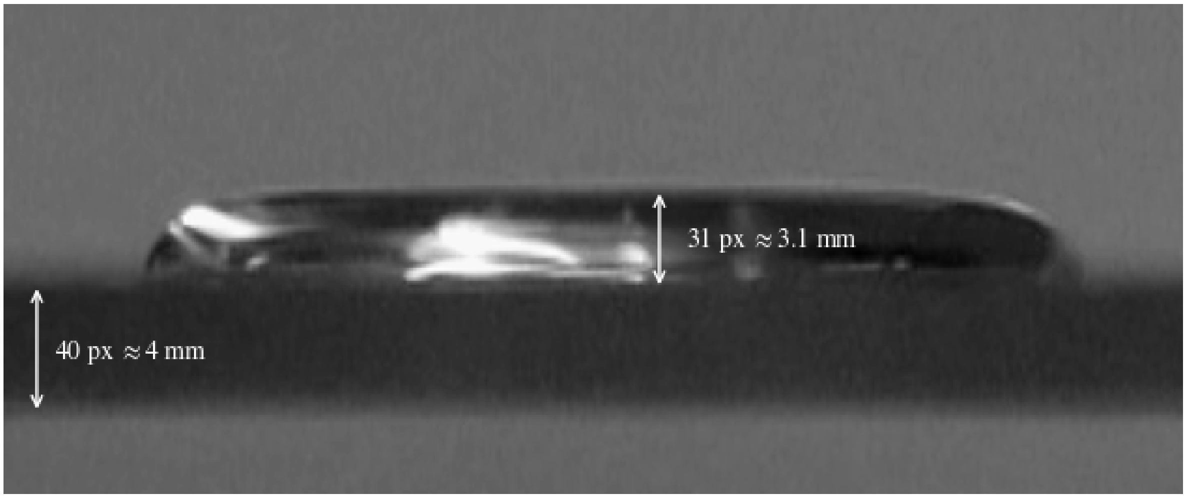

Figure 5. Shadowgraphic image for comparison with the presented measurement method. An additional calibration image in the imaging plane was used to calculate the film thickness. The additional thickness of the PMMA plate in thickness is presented for reference.

(a) reference and measurement image overlaid in one image

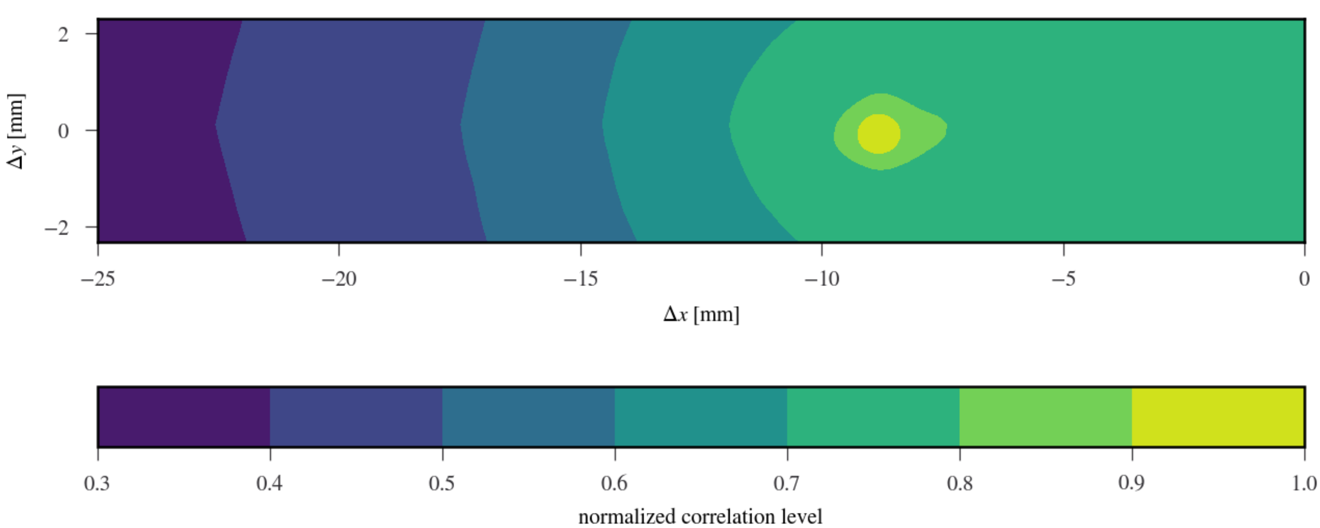

(b) correlation map between reference and measurement image

Figure 6. Measured images and correlation between them.

transform (FFT). This step is optional, yet decreases computation time significantly as compared to computing the cross-correlation in the image domain.

2. Compute the cross-correlation of the images.

3. Transform the computed correlation map back into the space domain via the two-dimensional inverse FFT (Fig. 6b)(only required if 1. is chosen).

4. Determine the initial displacement estimation by finding the position of the maximum correlation value of the correlation map.

5. Refine the initial estimation to sub-pixel accuracy by fitting a paraboloid function to a square kernel of correlation values around the initial peak and computing the position of the paraboloids maximum.

A correlation peak in the center of the correlation map is the result of calculating the auto-correlation of an image and is therefore interpreted as a displacement of 0. Consequently, the position of the correlation peak relative to the correlation map center can be interpreted as the displacement of the beam between images, i.e.

$$\Delta s = \left(\Delta x^2 + \Delta y^2\right)^{\frac{1}{2}} . \tag{11}$$

Applying this method to the example data set yields a beam displacement on the camera of $\delta s = 171.1\,\text{px} = 7.92\,\text{mm}$, which translates to a film thickness of $h \approx 3.05\,\text{mm}$ utilizing Eq. (9).

The complete processing routine is built on the Python packages PIL for image handling and NumPy (Harris et al., 2020) and SciPy (Virtanen et al., 2020) for scientific computing. The processing of one image pair takes about $0.6\,\text{s}$ consistently on an Intel Core i5 $2.4\,\text{MHz}$ single core, meaning the processing can be run in real time at more than $1\,\text{Hz}$ while maintaining the ability to store images at a significantly higher rate for a more accurate post-processing evaluation based on the same methods.

5. Measurement Uncertainty

For the derivation of the working principle in Sec. 2 a number of assumptions were made. In this section, these assumptions are discussed and their consequences for the accuracy of the measurement technique are evaluated. The possible error sources are listed here in the order in which they occur when following the beam from the laser source to the scope.

In order to quantify and visualize the errors, the setup geometry has been defined with example values relative to the film thickness h_f as shown in Fig. 7 alongside the initial laser direction and the coordinate system. While an analytical determination of the error functions is possible, the resulting descriptions can become convoluted, especially for the cases in which three-dimensional

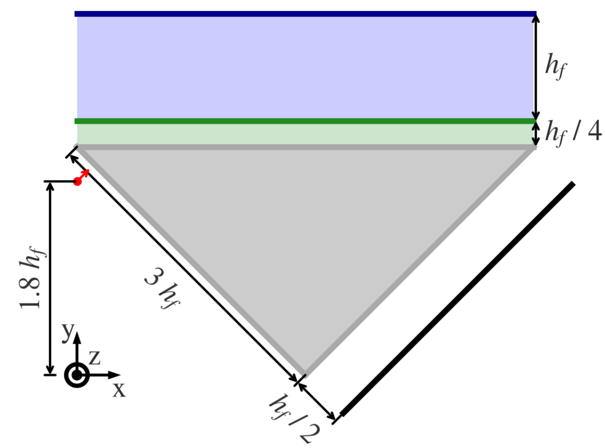

Figure 7. Dimensions and coordinate system used for the error discussion

effects need to be accounted for. The quantification of the errors was therefore done by implementing a simple ray-tracing routine based on the algorithm described in Sec. 2 Only especially remarkable cases are subsequently treated analytically.

The first assumption made is that the laser beam enters the prism orthogonally. However, it might even be desirable to have the beam enter at a slight angle to prevent reflections back into the laser source. Fig. 8a shows the effect of rotating the laser around the $(0\ 0\ 1)$ / z axis by an angle $-5^\circ \leq \delta\theta \leq 5^\circ$ before using the algorithm described in Sec. 2 to numerically compute its trajectory through the system. The dashed and dotted lines show the trajectories of the maximally displaced laser beams. The solid line depicts the unaltered reference case. Fig. 8c plots the relative measurement error as a function of the misalignment angle, where the error defined as the film thickness h estimated by the tracked beam compared to the prescribed film thickness h_0:

$$e_{\text{rel}} = 100\% \, \frac{h - h_0}{h_0}. \tag{12}$$

It is evident that a misalignment of only a few degrees causes a significant relative measurement error of multiple percentage points due to a change of the laser's optical path length within the film. The angle of incidence at the interface between transparent material and film is

$$\theta_{t,f} = \theta_{\text{prism}} + \delta\theta. \tag{13}$$

It is assumed that prism and transparent material have the same refractive index and therefore no refraction of the beam happens at their interface ($\theta_{p,t} \equiv \theta_{t,p}$). Inserting this definition in Eq. (6) yields

$$\theta_{f,t} = \frac{n_t}{n_f} \sin\theta_{t,f} = \frac{n_t}{n_f} \sin\left(\theta_{\text{prism}} + \delta\theta\right). \tag{14}$$

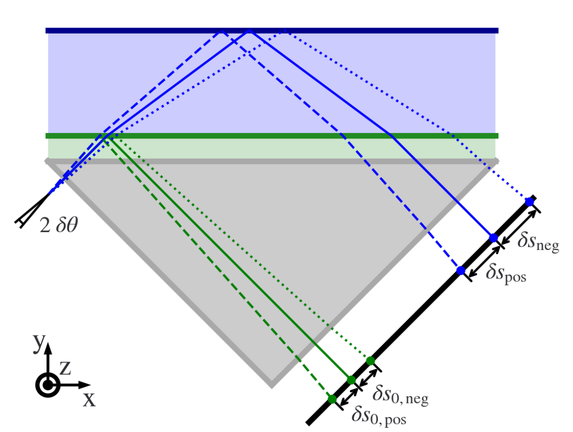

(a) beam trajectories caused by rotating the laser source around the $(0\ 0\ 1)$ direction; green: transparent surface; blue: film surface

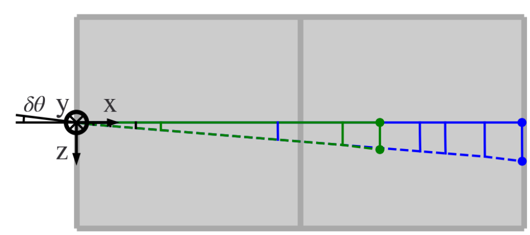

(b) beam trajectories caused by rotating the laser source around the $(-1\ 1\ 0)$ direction; green: transparent surface; blue: film surface; solid vertical lines: sites of refraction

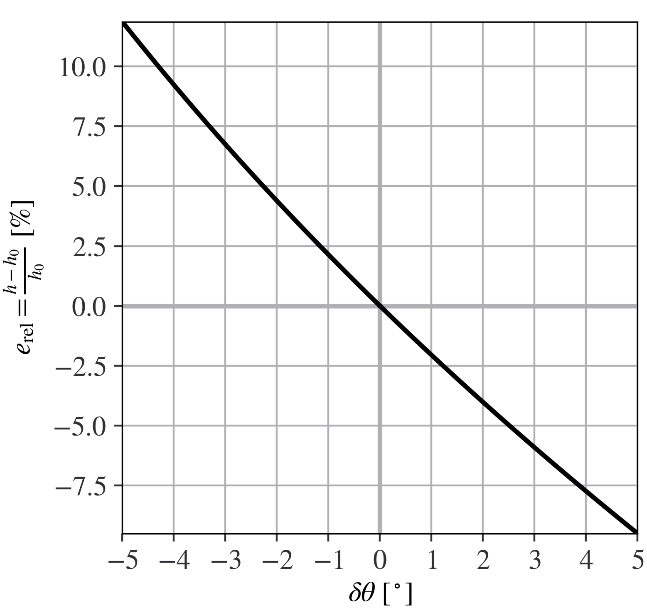

(c) error caused by rotating the laser around the $(0\ 0\ 1)$ direction

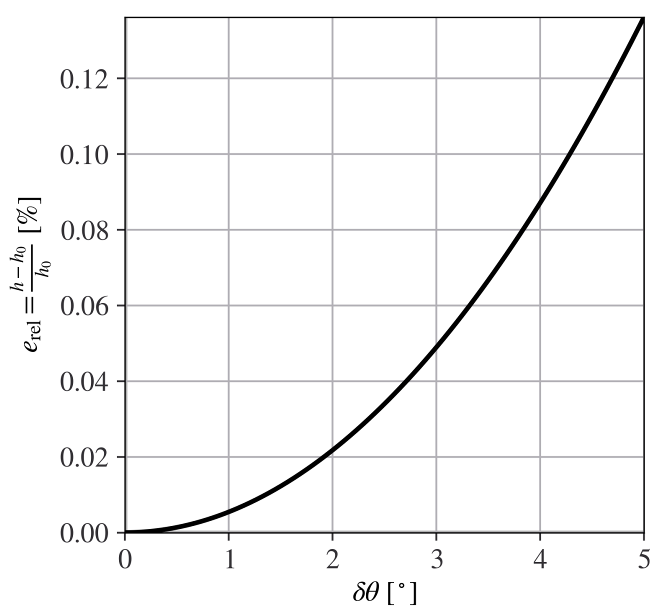

(d) error caused by rotating the laser around the $(-1\ 1\ 0)$ direction

Figure 8. Relative error caused by the laser meeting the prism's front surface at an angle.

Differentiating this result for $\delta\theta$, the relation

$$\frac{\partial \theta_{f,t}}{\partial \delta\theta} = \frac{n_t}{n_f} \cos\left(\theta_{\mathrm{prism}} + \delta\theta\right) \tag{15}$$

reveals that the systematic error by misalignment of the angle of incidence onto the prism is non-linear with respect to the angular deviation ($\delta s_{(0),\mathrm{pos}} < \delta s_{(0),\mathrm{neg}}$). When $\delta\theta$ is known, the error can be compensated via Eq. (14). Conversely, calibration with a known film thickness can yield $\Delta\theta$ assuming that all other error sources have been accounted for.

To avoid problems related to the reflection of the laser beam back in the laser source, it can also be rotated around the $(-1\ 1\ 0)$ axis. Again, the beam is rotated by $0 \leq \delta\theta \leq 5°$. Negative values are omitted due to the symmetry of the problem in this case. Fig. 8b displays the trajectory of maximum displacement with the dotted lines and the unaltered reference with solid lines. The quasi-vertical lines indicate the positions at which the laser beams cross optical surfaces. The significant displacement of the beam inside the xz plane does not influence the measurement results if only the projection of Δs in the xy plane is considered in Eq. (9). Still, refraction leads to a minor additional displacement in this projection as well, causing a measurement error. As shown in Fig. 8d, this error is smaller by orders of magnitude as compared to the rotation around the z axis.

While rotating the laser slightly around the $(-1\ 1\ 0)$ axis seems to be a good measure to prevent problems arising from the laser being reflected back, it must be remarked that introducing three-dimensionality into the measurement system significantly increases the complexity of predicting the effects of other error sources.

Since the reflected beams in presence and absence of the liquid film both exit the prism parallel to each other, the relative error does not change for different scope positions and for both rotations around the z or the $(-1\ 1\ 0)$ axis.

One key problem present when measuring liquid films is that the top surface of the film might not be parallel to the transparent-liquid interface, due to a curvature of the liquid-gas interface. The error introduced by a rotation of the top plane around the x or z axis is presented in Fig. 9. To quantify the error, the film's normal vector was rotated by an angle $\delta\theta$ before applying the ray-tracing algorithm to determine the beam trajectory numerically.

It is evident that, similar to the rotation of the laser source around the z axis, a rotation of the film surface around the same axis by $-4° < \delta\theta < 4°$ as depicted in Fig. 9a introduces a measurement error that might exceed 10% .

At a single interface, the error introduced by the rotation can be formulated as

$$\Delta x_{i,\mathrm{err}} = d_i \left[\tan\left(\theta_{i,j,\mathrm{err}}\right) - \tan\left(\theta_{i,j}\right)\right], \tag{16}$$

where d is the thickness of the respective layer, $\theta_{i,j}$ represents the angle of incidence and $\theta_{i,j,\mathrm{err}}$ represents the erroneous angle caused by misalignment. Therefore, the length of the optical path is a factor in the error and, hence, can be reduced by decreasing the dimensions of the prism and transparent material as well as the distance between prism and scope.

For static films, compensation via calibration is possible. The same is not true for dynamic films, where instantaneous values of film thickness are encumbered with a measurement uncertainty proportional to the standard deviation of the film's surface angle. Furthermore, for surface angles relative to the z axis of $\delta\theta < -4°$, the measurement principle is invalidated, since the angle of incidence $\theta_{f,a}$ is reduced until the condition for total reflection (see Eq. 5) is not met anymore.

Analogously, again, to the laser rotation, a rotation of the film surface around the x axis (depicted as seen in the yz projection in Fig. 9b) causes an error that is smaller by orders of magnitude as compared to a rotation around the z axis. Furthermore, a rotation around the x axis can only increase the angle of incidence and can therefore not jeopardize the working principle.

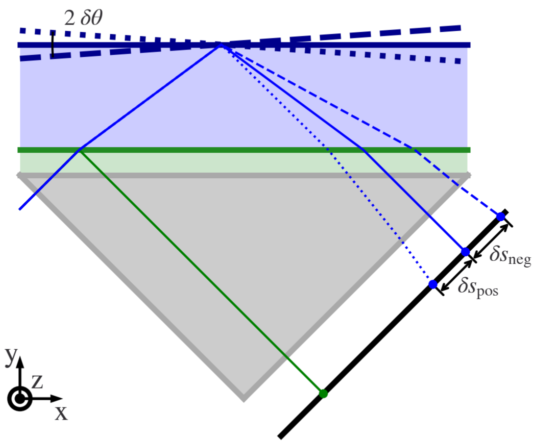

(a) beam trajectory caused by rotating the film surface around the $(0\ 0\ 1)$ direction; green: transparent surface; solid blue: straight film surface; dashed / dotted: film surface rotated by $\pm\delta\theta$

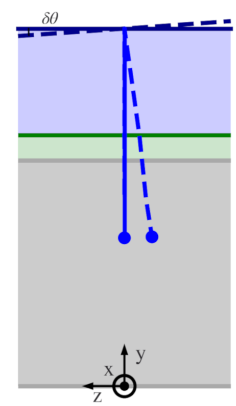

(b) beam trajectory caused by rotating the film surface around the $(1\ 0\ 0)$ direction; green: transparent surface; solid blue: straight film surface; dashed: film surface rotated by $\delta\theta$

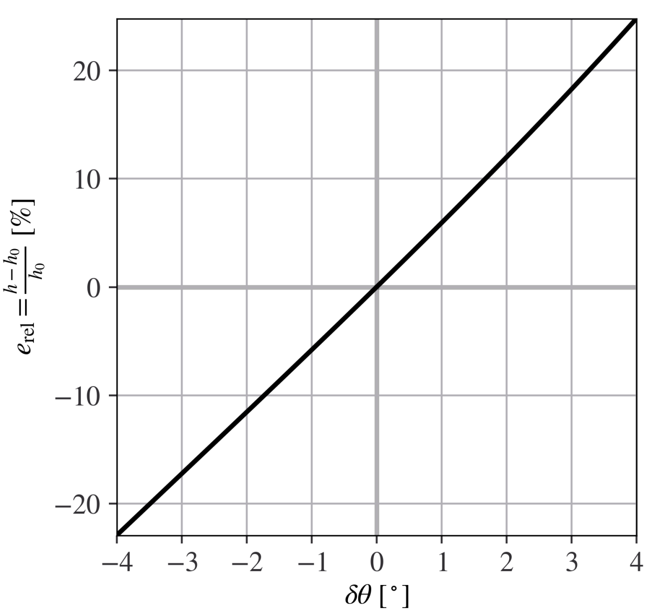

(c) error caused by a rotation of the film surface around the $(0\ 0\ 1)$ direction

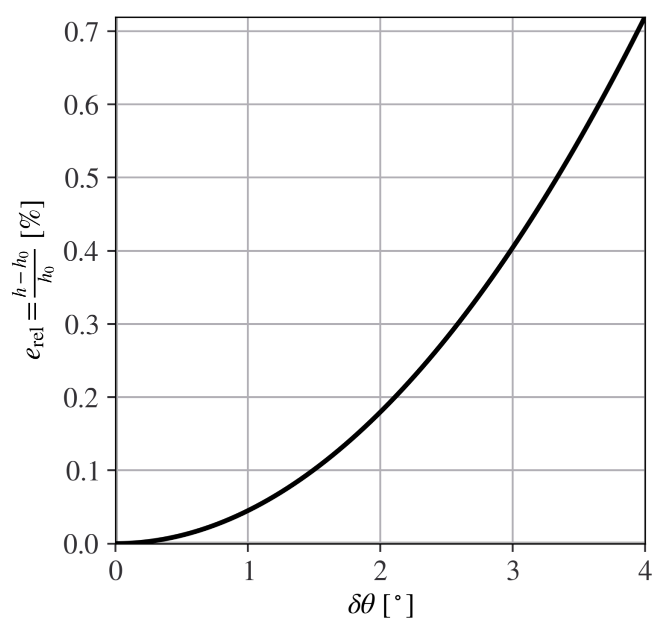

(d) error caused by a rotation of the film surface around the $(1\ 0\ 0)$ direction

Figure 9. Relative error caused by the film surface being non-parallel with its interface to the transparent material.

Another simplification was to assume the refractive indices of transparent material and prism to be equal. Different refractive indices of different materials for prism and glass substrate of course cause a deflection at the prism / transparent medium interface. For the exemplary combination of an optical window made of PMMA and a prism attached to it made from N-BK7, Snell's law leads to a deflection of

$$\frac{\sin\theta_{t,p}}{\sin\theta_{p,t}} = \frac{n_p\,(\lambda = 633\,\mathrm{nm})}{n_t\,(\lambda = 633\,\mathrm{nm})} \approxeq 1.0176 \tag{17}$$

for the applied He-Ne laser. The systematic error imposed on the theoretical beam-impact position on the scope can be compensated analytically using Eq. (17). However, this systematic error is constant for any given material pairing, causing the error to vanish in practice when comparing the beam's imprint on the scope to a reference point. Similarly, a possible glue layer that is used to fix a prism to an optical window / transparent material can be modeled as another transparent layer in which the beam is refracted and is therefore considered to be unproblematic. Nonetheless, it is advisable to find materials with closely matching refractive indices, since, as already mentioned, possible non-linear three-dimensional effects can cause beam deflections that get more difficult to predict with increasing system complexity.

Lastly, data recording and processing will introduce further uncertainties to the principle. As described in Sec. 4, an algorithm based on cross-correlation between a reference image and the measurement image is used to compute the laser beam displacement. Its core assumption is that the laser beam's imprint on the camera chip retains a self-similar shape between images. As long as this is accounted for, the algorithm finds the displacement peak within less than a pixel. For better understanding of the algorithm's accuracy, a study using a labeled test data set is required, which could be accomplished by synthetic image data.

One possible issue is the distortion of the laser beam's shape by a curved surface, consequently smearing the correlation peak. To counteract against, the beam diameter can be decreased with suitable lenses. Note however, that increased camera resolution will also increases the spatial accuracy of displacement detection.

6. Conclusions and Outlook

In this work, the Laser Pattern Shift Method (Foltyn et al., 2019) for film thickness measurement utilizing total reflection was investigated with respect to the application to dynamic film flows. The method is non-intrusive and requires only minimal optical access from below the interface between the optical window and the film. Mechanical access is not required for the measurements. Therefore, the technique can be used to investigate films in measurement setups that have very limited possibilities for modification.

A three-dimensional linear algebra model for the measurement technique, based on geometrical optics, was derived to facilitate error estimations. It was shown in a proof-of-concept setup that the theoretically derived measurement principle predicted the thickness of a static water film accurately in sample measurements, and is therefore expected to be generally applicable where optical access is possible and the investigated film is transparent.

Rotations of the laser beam or the film's surface around the system's z axis prove to be a source of high measurement errors that can be compensated via calibration in the case of static films. However, for dynamic films with a strongly curved surface, instantaneous film thickness data is likely not reliable. Further work should include the investigation of the reliability of time-averaged film thickness data for different dynamic film flows. Rotation around the x or $(1\ -1\ 0)$ direction showed to cause errors that are smaller by orders of magnitude.

A robust and ready for real-time processing algorithm based on image cross-correlation was presented. The assumption of self-similarity of the beam shape between images - which is the basis for this algorithm - needs to be validated in the future.

References

Ameur, M. A., Stutz, B., & Lallemand, M. (2007, October). Unsteady Natural Convective Boiling in a Narrow Vertical Channel. *Heat Transfer Engineering*, *28*(10), 870–876.

Aussillous, P., & Quéré, D. (2000, October). Quick deposition of a fluid on the wall of a tube. *Physics of Fluids*, *12*(10), 2367–2371.

Barbosa Jr, J., Govan, A., & Hewitt, G. (2001, December). Visualisation and modelling studies of churn flow in a vertical pipe. *International Journal of Multiphase Flow*, *27*, 2105–2127.

Blessing, S. (2022, May). *Total Reflective Film Thickness Processing.* doi: 10.5281/zenodo.6603680

Burns, J. R., Ramshaw, C., & Jachuck, R. J. (2003, June). Measurement of liquid film thickness and the determination of spin-up radius on a rotating disc using an electrical resistance technique. *Chemical Engineering Science*, *58*(11), 2245–2253.

Busam, S., Ebner, J., & Wittig, S. (2001, 06). An Experimental Study of Liquid Film Thickness in Annular Air/Oil Flow in a Vertical Pipe Using a Laser Focus Displacement Meter. In (Vol. Volume 3: Heat Transfer; Electric Power; Industrial and Cogeneration).

Coney, M. W. E. (1973, September). The theory and application of conductance probes for the measurement of liquid film thickness in two-phase flow. *Journal of Physics E: Scientific Instruments*, *6*(9), 903–911.

Foltyn, P., Rihm, L. K., Ribeiro, D., Silva, A., & Weigand, B. (2021, October). Measurement of the lamella thickness during droplet impact onto differently wettable smooth surfaces using an extension of the LASER Pattern Shift Method with naturally occurring patterns. *Review of Scientific Instruments*, *92*(10), 105111.

Foltyn, P., Roth, N., & Weigand, B. (2019). Development and calibration of the laser pattern shift method for measuring the lamella topology during drop impact on walls..

Fukano, T. (1998, August). Measurement of time varying thickness of liquid film flowing with high speed gas flow by a constant electric current method (CECM). *Nuclear Engineering and Design*, *184*(2), 363–377.

Han, Y., & Shikazono, N. (2009, October). Measurement of the liquid film thickness in micro tube slug flow. *International Journal of Heat and Fluid Flow*, *30*(5), 842–853.

Han, Y., & Shikazono, N. (2010, August). The effect of bubble acceleration on the liquid film thickness in micro tubes. *International Journal of Heat and Fluid Flow*, *31*(4), 630–639.

Han, Y., Shikazono, N., & Kasagi, N. (2011, January). Measurement of liquid film thickness in a micro parallel channel with interferometer and laser focus displacement meter. *International Journal of Multiphase Flow*, *37*(1), 36–45.

Harris, C. R., Millman, K. J., van der Walt, S. J., Gommers, R., Virtanen, P., Cournapeau, D., … Oliphant, T. E. (2020, September). Array programming with NumPy. *Nature*, *585*(7825), 357–362.

Hazuku, T., Fukamachi, N., Takamasa, T., Hibiki, T., & Ishii, M. (2005, June). Measurement of liquid film in microchannels using a laser focus displacement meter. *Experiments in Fluids*, *38*(6), 780–788.

Hurlburt, E. T., & Newell, T. A. (1996, September). Optical measurement of liquid film thickness and wave velocity in liquid film flows. *Experiments in Fluids*, *21*(5), 357–362.

Kang, H. C., & Kim, M. H. (1992, May). The development of a flush-wire probe and calibration method for measuring liquid film thickness. *International Journal of Multiphase Flow*, *18*(3), 423–437.

Klausner, J. F., Zeng, L. Z., & Bernhard, D. M. (1992, May). Development of a film thickness probe using capacitance for asymmetrical two-phase flow with heat addition. *Review of Scientific Instruments*, *63*(5), 3147–3152.

Kumar, R., Gottmann, M., & Sridhar, K. (2002). Film Thickness and Wave Velocity Measurements in a Vertical Duct. *Journal of Fluids Engineering*.

Liu, S., Li, J., & Chen, Q. (2007, June). Visualization of Flow Pattern in Thermosyphon by ECT. *AIP Conference Proceedings*, *914*(1), 775–785.

Lu, Q., Suryanarayana, N. V., & Christodoulu, C. (1993, November). Film thickness measurement with an ultrasonic transducer. *Experimental Thermal and Fluid Science*, *7*(4), 354–361.

Lubnow, M., Dreier, T., Schulz, C., & Endres, T. (2021, November). Simultaneous measurement of liquid-film thickness and solute concentration of aqueous solutions of two urea derivatives using NIR absorption. *Applied Optics*, *60*(32), 10087–10093.

Makarytchev, S. V., Langrish, T. A. G., & Prince, R. G. H. (2001, January). Thickness and velocity of wavy liquid films on rotating conical surfaces. *Chemical Engineering Science*, *56*(1), 77–87.

Moriyama, K., & Inoue, A. (1996, February). Thickness of the Liquid Film Formed by a Growing Bubble in a Narrow Gap Between Two Horizontal Plates. *Journal of Heat Transfer*, *118*(1), 132–139.

Mouza, A. A., Vlachos, N. A., Paras, S. V., & Karabelas, A. J. (2000, April). Measurement of liquid film thickness using a laser light absorption method. *Experiments in Fluids*, *28*(4), 355–359.

Peatross, J., & Ware, M. (2021). *Physics of light and optics*. available at optics.byu.edu.

Pedersen, P. C., Cakareski, Z., & Hermanson, J. C. (2000, March). Ultrasonic monitoring of film condensation for applications in reduced gravity. *Ultrasonics*, *38*(1), 486–490.

Peterson, J. P., & Peterson, R. B. (2006, July). Laser triangulation for liquid film thickness measurements through multiple interfaces. *Applied Optics*, *45*(20), 4916–4926.

Porter, J. M., Jeffries, J. B., & Hanson, R. K. (2011, February). Mid-infrared laser-absorption diagnostic for vapor-phase fuel mole fraction and liquid fuel film thickness. *Applied Physics B: Lasers and Optics*, *102*, 345–355. (ADS Bibcode: 2011ApPhB.102..345P)

Salazar, R. P., & Marschall, E. (1975, November). Thickness measurement in liquid film flow by laser scattering. *Review of Scientific Instruments*, *46*(11), 1539–1541.

Schmidt, A., Bonarens, M., Roisman, I. V., Nishad, K., Sadiki, A., Dreizler, A., … Wagner, S. (2021, January). Experimental Investigation of AdBlue Film Formation in a Generic SCR Test Bench and Numerical Analysis Using LES. *Applied Sciences*, *11*(15), 6907.

Schulz, F., Samenfink, W., Schmidt, J., & Beyrau, F. (2016, May). Systematic LIF fuel wall film investigation. *Fuel*, *172*, 284–292.

Seleghim, P., & Hervieu, E. (1998, September). Direct imaging of two-phase flows by electrical impedance measurements. *Measurement Science and Technology*, *9*(9), 1492–1500.

Shedd, T. A., & Newell, T. A. (1998, December). Automated optical liquid film thickness measurement method. *Review of Scientific Instruments*, *69*(12), 4205–4213.

Steinbrenner, J. E., Hidrovo, C. H., Wang, F.-M., Vigneron, S., Lee, E. S., Kramer, T. A., … Goodson, K. E. (2007, July). Measurement and modeling of liquid film thickness evolution in stratified two-phase microchannel flows. *Applied Thermal Engineering*, *27*(10), 1722–1727.

Suo, M., & Griffith, P. (1964, September). Two-Phase Flow in Capillary Tubes. *Journal of Basic Engineering*, *86*(3), 576–582.

Takahama, H., & Kato, S. (1980, June). Longitudinal flow characteristics of vertically falling liquid films without concurrent gas flow. *International Journal of Multiphase Flow*, *6*(3), 203–215.

Takamasa, T., & Kobayashi, K. (2000, September). Measuring interfacial waves on film flowing down tube inner wall using laser focus displacement meter. *International Journal of Multiphase Flow*, *26*(9), 1493–1507.

Than, C. F., Tee, K. C., Low, K. S., & Tso, C. P. (1993, March). Optical measurement of slope, thickness and velocity in liquid film flow. *Smart Materials and Structures*, *2*(1), 13–21.

Triplett, K. A., Ghiaasiaan, S. M., Abdel-Khalik, S. I., & Sadowski, D. L. (1999, April). Gas–liquid two-phase flow in microchannels Part I: two-phase flow patterns. *International Journal of Multiphase Flow*, *25*(3), 377–394.

Ursenbacher, T., Wojtan, L., & Thome, J. R. (2004, February). Interfacial measurements in stratified types of flow. Part I: New optical measurement technique and dry angle measurements. *International Journal of Multiphase Flow*, *30*(2), 107–124.

Virtanen, P., Gommers, R., Oliphant, T. E., Haberland, M., Reddy, T., Cournapeau, D., … SciPy 1.0 Contributors (2020). SciPy 1.0: Fundamental Algorithms for Scientific Computing in Python. *Nature Methods*, *17*, 261–272.

Wigger, S., Füßer, H.-J., Fuhrmann, D., Schulz, C., & Kaiser, S. A. (2016, January). Quantitative two-dimensional measurement of oil-film thickness by laser-induced fluorescence in a piston-ring model experiment. *Applied Optics*, *55*(2), 269–279.

Yu, S. C. M., Tso, C. P., & Liew, R. (1996, July). Analysis of thin film thickness determination in two-phase flow using a multifiber optical sensor. *Applied Mathematical Modelling*, *20*(7), 540–548.

Åkesjö, A., Vamling, L., Sasic, S., Olausson, L., Innings, F., & Gourdon, M. (2018, December). On the measuring of film thickness profiles and local heat transfer coefficients in falling films. *Experimental Thermal and Fluid Science*, *99*, 287–296.